IEEE Access
Multidisciplinary ⋮ Rapid Review ⋮ Open Access Journal

Received 4 March 2024, accepted 16 March 2024, date of publication 25 March 2024, date of current version 1 April 2024.

Digital Object Identifier 10.1109/ACCESS.2024.3380446

RESEARCH ARTICLE

An MPC-Based Algorithm for Estimating the Spatial DNI of Cloud Shaded Regions Using a Robotic Sensor System

JOSÉ M. AGUILAR-LÓPEZ, RAMÓN A. GARCÍA, AND EDUARDO F. CAMACHO, (Life Fellow, IEEE)
Departamento de Ingeniería de Sistemas y Automática, Universidad de Sevilla, 41092 Seville, Spain

Corresponding author: José M. Aguilar-López (jaguilarl@us.es)

This work was supported by European Research Council (ERC) under European Union's Horizon 2020 Research and Innovation Program under the advanced grant Optimal CONTrol of Thermal SOLAR energy systems (OCONTSOLAR) under Grant 789051.

ABSTRACT This paper presents an original algorithm based on the Model Predictive Control strategy for estimating the direct normal irradiance of cloud shaded regions using a mobile robotic sensor system to improve the control of a solar thermal power plant. This new algorithm generates the waypoints of the robot team solving a minimisation problem where the objective function combines several criteria, including the measurements taken by the team. The novel method has been tested by simulation with groups of different numbers of unmanned aerial vehicles using the shape of real cloud shadows projected on the ground extracted from images and it improves the estimation error and the estimation time of previous algorithms.

INDEX TERMS DNI, robotic sensor system, solar energy, spatial solar radiation estimation, UAV.

I. INTRODUCTION

Climate change is one of the biggest challenges of this century. Greenhouse gases are one of the main causes of climate change [1]. The problem is that carbon emissions are linked to economic growth [2], so a balance must be struck between producing energy in a way that is not harmful to the environment and economic growth. The most affordable way to achieve this goal is through renewable energy [3], which requires increasing the efficiency of this alternative energy source.

Among renewable energy sources, solar energy is one of the best choices, as the sun continuously radiates energy to the earth. Solar energy can be converted into electricity directly through photovoltaic (PV) cells or indirectly through concentrated solar power (CSP) systems. Many solar plants have been built in recent decades [4], and the European Commission has recognised the need to increase their competitiveness [5].

The main disadvantage of obtaining energy from solar radiation is its strong dependence on weather and climate conditions [6], which makes solar radiation variable. The theoretical solar radiation received can be predicted with physical models using latitude and longitude, date, and hour [7]. However, there are other factors, such as meteorological ones, that are unpredictable. The blocking effect of the passing clouds affects the intensity of solar radiation and thus the production of electrical energy. This attenuation can easily reach 50% of the solar radiation [8].

Large variations in direct normal irradiance (DNI) are counterproductive in a solar thermal power plant, since its operation depends on maintaining the average temperature of the field around the set point [9]. Knowing the spatial distribution of the DNI and varying the operating temperature accordingly has been shown to increase energy production and, consequently, the economic benefits [10]. This work covers part of the objectives of the European Research Council in the Advanced Grant OCONTSOLAR [11], specifically the design of methods to control the mobile sensor fleet as part of the control system, and the design of spatially distributed solar irradiance

The associate editor coordinating the review of this manuscript and approving it for publication was Fei Chen.

estimation methods using this fleet. Other research has also studied the estimation of the spatial distribution of DNI, or algorithms to improve the control of solar plants with these estimations [12].

Reference [13] describes the use of cameras to create an irradiance map through shadow detection. Other research uses sensors, as in [14], where photovoltaic panels are used as irradiance sensors and their data are fused with fixed DNI sensors to provide a spatial DNI measurement. In the last decade, unmanned aerial vehicles (UAVs) have become increasingly popular and their use has been extended to various fields such as 3D geomatic mapping [15] or precision agriculture [16]. UAVs have already been used in solar power plants, but mainly for maintenance purposes [17].

This paper proposes a new method to characterise the variations in DNI caused by clouds passing in the vicinity of a concentrated solar power plant, as this information is critical for the plant's control system to operate in the most efficient manner. The main contribution of this work is an original algorithm based on a Model Predictive Control (MPC) strategy to manage a robotic sensor system (RSS) composed of several UAVs to collect DNI information. The waypoints of the RSS are generated using an algorithm based on a Model Predictive Control (MPC) strategy that combines several criteria, such as measurement uncertainty and energy consumption, among others. The measurements are carried out by lightweight and low energy consumption sensors mounted on the UAVs and are used to estimate the DNI of the area using the Delauney triangulation. This proposal has been tested by simulation using the shape of real cloud shadows projected on the ground and extracted from images, and compared with a previous algorithm, improving both the estimate obtained and the time to converge to the final estimate.

This paper is structured as follows. Section II describes the problem under consideration. Section III presents the proposed solution, which is tested by simulations in Section IV. Finally, some conclusions and remarks are given in Section V.

II. PROBLEM OVERVIEW

A. AREA DESCRIPTION AND WIND ASSUMPTIONS

In this work, the region of interest (ROI) is an area A adjacent to the area where the solar power plant is located. This ROI is defined as:

$$A \equiv (x, y)/x \in [x_{inf}, x_{sup}], y \in [y_{inf}, y_{sup}], \qquad (1)$$

where $x_{inf}, x_{sup}, y_{inf}, y_{sup}$ are the width and length boundaries, respectively. The ROI is divided into a grid of $M \times N$ cells to store the DNI measurements and the estimates made from them. The exact location of A depends on the wind direction, as the clouds are assumed to move in the same direction as the wind. Fig. 1 shows an example of the area description. Wind information is provided by anemometers placed at ground level in the area. It can be adjusted for cloud height using the equation 2:

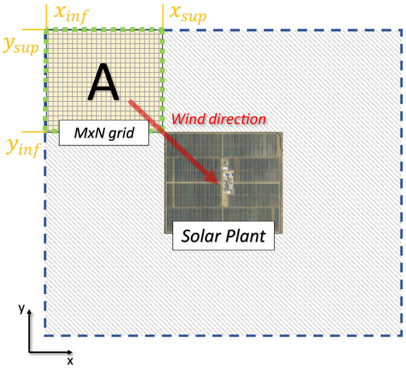

FIGURE 1. Area description and example of location by wind direction.

$$v_h = v_{h_0}\left(\frac{h}{h_0}\right)^{1/\alpha}, 0 < h < h_0, \qquad (2)$$

described in [18], where v_h, v_{h_0} are the wind speed at height h, h_0 respectively, and α is the wind shear exponent coefficient, which reflects how the wind speed increases with height. Generally, $\alpha = 0.143$ in open fields. In this case h_0 is the ground and h is the cloud base height. This height can be estimated using stereo vision with two sky cameras as shown in [19], or using a ceilometer, such as [20], to measure cloud base distances. As the weather, wind direction, and speed can change and the accuracy of predictions decreases over time, we are consider short time horizons of 5 to 30 minutes.

B. ROBOTIC SENSOR SYSTEM

The RSS is defined as a set of n_u UAVs:

$$U = \{u_1, u_2, \ldots, u_{n_u}\}, \qquad (3)$$

which are deployed in the field. The fleet is commanded by a ground station computer that is able to receive the data collected by the multi-UAV system, fuse them, decide the next waypoints by running the algorithm described in this paper, and command the new waypoints to the fleet. The UAVs are equipped with a low energy consumption sensor to measure DNI, such as the [21] shown in Fig. 2. This sensor is mounted on a gimbal to point directly at the sun and measure the DNI, as can be seen in Fig. 2b. Spencer's equations [22] can be used to point at the sun at any time. The sensor's radiation accuracy is better the closer it is to the sun's normal vector, but the error is less than 10% according to the manufacturer. Although the sampling frequency of the sensor is 50 Hz, in this work we assume that each measurement is the average of the last 5 measurements taken, in order to filter out the noise and reduce the error. Therefore, the final sampling frequency is 10 Hz. To avoid collisions, each UAV flies at an operating altitude h^{ref} 5 metres different from the previous and the next, i.e.:

$$h^{ref}_{i+1} - h^{ref}_i = 5, \quad \forall i = 1, 2, \ldots, n_u. \qquad (4)$$

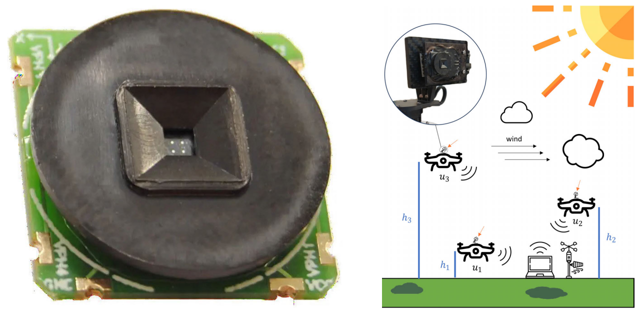

(a) Sun sensor from Solar Mems. (b) Scenario illustration.

FIGURE 2. Icons images from Flaticon.com.

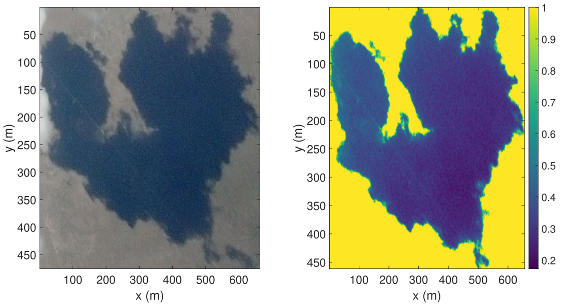

FIGURE 3. Example of cloud shape and sun-blocking values extracted from images.

In Fig. 2b a scheme of the scenario is shown. Finally, it is assumed that they can move at a constant average speed of commercial drones such as *DJI Phantom 3* [23]. We have assumed 8 m/s for horizontal movement, and 2 m/s for vertical movement.

C. CLOUDS SHAPE AND BLOCKING EFFECT

To compensate for the lack of real cloud data, we have used photographs of cloud shadows projected onto the ground. The shape of the clouds is extracted from these images, ranging from relatively elliptical shapes to highly concave ones and with multiple holes. The sun-blocking properties of a cloud depend mainly on its optical depth and vertical extent, as described in [24]. These parameters are difficult to obtain without sensors such as ceilometers, and also vary with time and are strongly dependent on weather conditions such as temperature, humidity or pressure [25]. As the operational time of UAVs is typically around 25-30 minutes, this work assumes that cloud characteristics remain constant during this time frame. This is because significant weather changes are unlikely to occur in such a short period of time. To generate a sun-blocking value for each position of the cloud shape, we have analysed the colour intensity of each pixel in the images and compared it to an unshaded pixel assigning values between 0 and 1. A value of 1 means that the sky is clear, whereas a value of 0 means that the entire DNI is blocked. An example of the cloud shape and sun-blocking values obtained are shown in Fig. 3.

III. PROPOSED SOLUTION

A. VARIABLES AND DESCRIPTION OF THE SOLUTION ALGORITHM

The proposed solution implements the Algorithm depicted in Fig. 4 and described below, which controls the behaviour of the RSS.

Consider the aforementioned set U of n_u UAVs. The position of any u_i UAV is given by:

$$pos_i = [l_i, L_i, h_i], \tag{5}$$

where l_i, L_i, h_i are latitude, longitude, and altitude, respectively. The operating altitude of each UAV, i.e., the height at which u_i must fly, is h_i^{ref}. In addition, each UAV has a list of waypoints that are updated by the algorithm, defined as:

$$\begin{aligned} W &= \{w_1, w_2, \ldots, w_{n_u}\}, \\ w_i &= \{wp_{i1}, wp_{i2}, \ldots, wp_{im_i}\}, \end{aligned} \tag{6}$$

where w_i is the list of m_i waypoints wp_{ij} of u_i. Each measurement taken by the UAVs is compared to a threshold R_{cs}, which takes the value of the clear sky radiation. This value can be determined using a fixed sensor such as a pyrheliometer pointed at the sun. Taking into account the maximum possible error of the UAV-mounted sensor, any reading below 10% R_{cs} is classified as a cloud point. A set of detected cloud points is made up of the measurements taken by the fleet following the waypoints of W. This set is defined as:

$$\Theta = \{(pos_k, I_k, t_k)\}, \tag{7}$$

where I_k is the irradiance value and t_k is the timestamp of the measurement taken by the UAV k at the position pos_k.

The algorithm uses the following variables:

- ϕ_i is boolean and indicates whether u_i needs a new set of waypoints w_i.
- Λ_i is boolean and indicates whether u_i needs to explore deeper into the current region. This is necessary to discard false positives and to ensure that the last measurement below the radiation threshold R_{cs} really belongs to a cloud shaded region.
- The variables γ and Γ indicate which UAV has to describe the cloud boundary counterclockwise or clockwise, respectively, or zero if no UAV is assigned.
- Δ is boolean and it indicates when the boundary is sufficiently described.

The algorithm can be summarised by repeating these steps:

a) Generate a new waypoint list w_i for each u_i, if necessary.
b) Assign a waypoint wp_{ij} from w_i to each u_i, if necessary.
c) Each u_i follows its assigned waypoint wp_{ij}.
d) Update both the set of detected cloud points Θ and the data maps with the new measurements taken.

B. DESCRIPTION OF THE ALGORITHM'S DATA MAPS

There are 3 different types of data map. All of them divide the area of interest into a matrix of 5 × 5 metre cells, but each

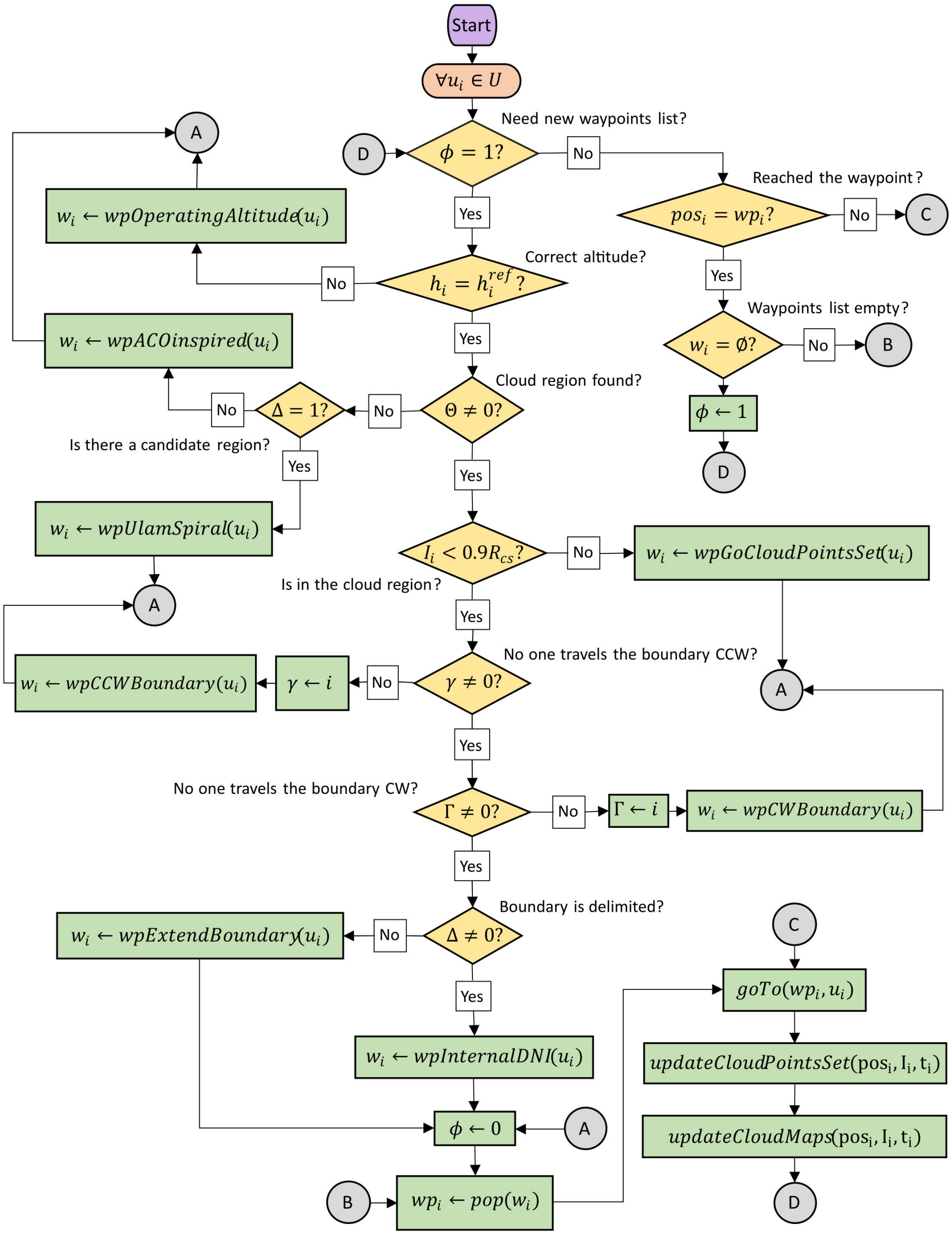
Start
$\forall u_i \in U$
Need new waypoints list?
D
$\phi = 1?$
No
Yes
A
$w_i \leftarrow wpOperatingAltitude(u_i)$
Reached the waypoint?
$pos_i = wp_i?$
No
C
Yes
Correct altitude?
No
$h_i = h_i^{ref}?$
Yes
Waypoints list empty?
$w_i \leftarrow wpACOinspired(u_i)$
$w_i = \emptyset?$
No
B
$\phi \leftarrow 1$
D
Cloud region found?
$\Theta \neq 0?$
No
$\Delta = 1?$
No
Is there a candidate region?
Yes
Yes
$w_i \leftarrow wpUlamSpiral(u_i)$
$I_i < 0.9R_{cs}?$
No
$w_i \leftarrow wpGoCloudPointsSet(u_i)$
Is in the cloud region?
A
Yes
No one travels the boundary CCW?
$w_i \leftarrow wpCCWBoundary(u_i)$
$\gamma \leftarrow i$
No
$\gamma \neq 0?$
A
Yes
No one travels the boundary CW?
$\Gamma \neq 0?$
No
$\Gamma \leftarrow i$
$w_i \leftarrow wpCWBoundary(u_i)$
Yes
Boundary is delimited?
$w_i \leftarrow wpExtendBoundary(u_i)$
No
$\Delta \neq 0?$
C
Yes
$goTo(wp_i, u_i)$
$w_i \leftarrow wpInternalDNI(u_i)$
$updateCloudPointsSet(\mathrm{pos_i}, \mathrm{I_i}, \mathrm{t_i})$
$\phi \leftarrow 0$
A
$updateCloudMaps(\mathrm{pos_i}, \mathrm{I_i}, \mathrm{t_i})$
B
$wp_i \leftarrow pop(w_i)$
D

FIGURE 4. **Flowchart of the algorithm.**

one stores different information. These maps are constantly updated as the UAVs take new measurements. The three are described below and shown in Fig. 5.

1) **DNI map:** stores the DNI measurements taken by the RSS in the area of interest. It is depicted in Fig. 5, on the left.
2) **Certainty map:** stores values between 0 and 1. Each cell indicates how reliable the measurement stored in the same cell of the DNI map is. A 0 means that no measurement has been taken; a 1 means that the DNI value corresponds to a measurement that has just been taken; any other intermediate value means that the DNI value corresponds to a measurement that was taken some time ago and its accuracy cannot be guaranteed. The lower the value, the less reliable it is. This reduction in confidence follows an exponential forgetting factor rule:

$$C_t = C_0 e^{-\lambda t}, \tag{8}$$

where C_0 is the original value of a cell in the certainty map, C_t its value after t seconds, and λ is the forgetting factor. The forgetting factor is adjusted in this paper to reduce the certainty to 0.5 after 60 seconds.
This map is shown in the middle of Fig. 5.

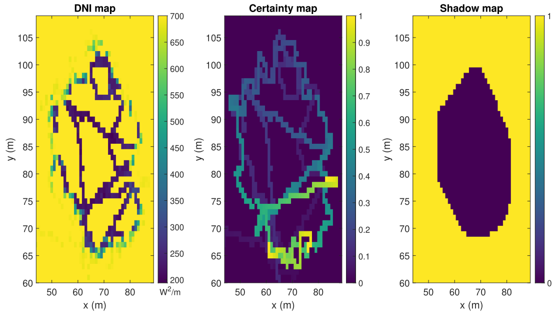

FIGURE 5. Example of data maps. From left to right: DNI map, certainty map, and shadow map.

3) **Shadow map:** determines which locations are in the shadow of the cloud and which are not. To create this map, all the low-DNI measurement positions are taken to obtain a convex polygon. This polygon represents the estimated area of the cloud shadow. The map cells inside the polygon are marked with 0 and those outside the polygon are marked with 1. This can be seen in Fig. 5, on the right.

C. WAYPOINTS GENERATION

There are three sets of waypoints generation functions in the algorithm. Each set has different objectives.

1) OPERATIONAL ALTITUDE

As it was mentioned in Section II, each UAV u_i has been assigned a safety operating altitude h_i^{ref}. The first set of waypoints only has the *wpOperatingAltitude* function, which is responsible for returning the w_i to carry u_i to h_i^{ref}.

2) SEARCHING THE CLOUD SHADED REGIONS

The second subset is responsible for finding the cloud shaded regions, namely, regions with low DNI values. For this task, this work uses an improved version of the algorithm described in a previous work by the authors [26]. These changes speed up the delineation of the low-DNI region boundary. In the previous work, all UAVs followed the boundary in a clockwise direction. Now, the first UAV is the only one with this behaviour. The second follows the boundary counterclockwise. The others, if any, extend the boundaries of the polygon already detected. To do this, the less explored boundaries of the polygon are selected and the UAVs fly through them following the gradient vector of the DNI, i.e., from the lower DNI values inside the shadow region to the higher ones in the outer region. In this way, the UAVs push out the boundaries of the estimated low-DNI polygon. The functions that implement this behaviour in the algorithm are *wpUlamSpiral*, *wpACOinspired*, *wpCCWBoundary*, *wpCWBoundary*, *wpExtendBoundary*, and *wpGoCloudPointsSet*, which are explained in the cited work except for the modifications mentioned above.

TABLE 1. Objective function weights.

	λ_1	λ_2	λ_3	λ_4	λ_5
Inside the shaded area	0.05	0.6	0.2	0.1	0.05
Outside the shaded area	0.09	0.2	0.6	0.1	0.01

3) DESCRIBING THE CLOUD SHADED REGIONS

The last subset is responsible for describing the spatial radiation of the cloud shaded regions. This paper presents a new procedure to generate the waypoints list w_i for each UAV u_i. This method is inspired by a Model Predictive Control (MPC) strategy in which a minimisation problem is solved to obtain the control signals for a time window, and only a few or only one control signals is applied in a receding control manner. The problem is formulated in the Equation 9, as shown at the bottom of the next page, where ν is the module of the UAVs speed, and λ_i is the weight of each term of the objective function. The function *wpInternalDNI* solves this minimisation problem to return the waypoints list w_i of each UAV u_i but, equivalent to the control signals of the MPC strategy, only the first waypoints are travelled. This is repeated periodically to get enough measurements to describe the DNI values of the region.

The decision variables of this problem are the angles θ_i. These angles determine the turn that each UAV u_i will make on its trajectory. In this paper, the time window or prediction horizon is defined as $N_1 = 0$ s and $N_2 = 10$ s, whereas the control horizon is defined as $N_u = 3$ s. The values of the weights λ_i of the objective function have been set heuristically after 1000 tests over 5 different cases with the properties described in Section IV and take their values from the Table 1, depending on whether u_i is inside the shaded area or not. For clouds that differ significantly from this configuration, e.g. with a higher velocity, these weights should be adjusted. Once the minimisation problem is solved and θ_i are selected for a time window, the waypoint lists w_i is computed for each u_i. Fig. 6 shows part of this process. The solution to the minimisation problem is obtained using an ad hoc Monte Carlo method, explained later.

The terms of the objective function are described as follows:

1) **DNI criterion:** $M_I(\theta_i)$ uses the DNI map to sum the DNI values of the places visited after applying θ_i. As regions with low DNI values are more interesting than regions with high DNI values, the lower the result, the better the waypoints are.
2) **Certainty criterion:** $M_C(\theta_i)$ uses the certainty map in the same way that $M_I(\theta_i)$ uses the DNI map. Since low certainty values come from unexplored regions or regions visited some time ago, the lower the value, the better the waypoints are.
3) **Boundary criterion:** $M_B(\theta_i)$ uses the shadow map in the same way as before. As regions inside the polygon boundaries are more interesting than those outside, the lower the value, the better the waypoints are.

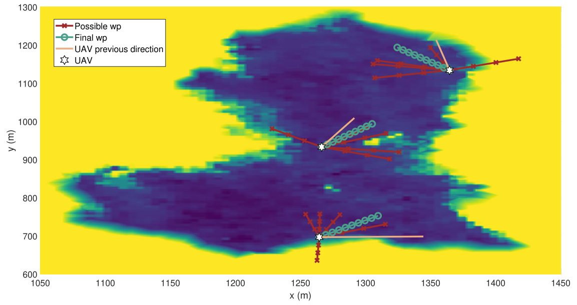

FIGURE 6. Example of the generation of the waypoints list w_i. The orange lines are the previous movement direction of each UAV u_i, i.e., the future movement if they didn't change their trajectory. When the angles θ_i are randomly generated, they define new trajectories that rotate the previous direction of movement, shown as red lines with crosses. Only a few possible waypoints are shown here. The final chosen waypoints of each UAV are shown as green circles.

4) **Efficiency criterion:** $T(\theta_i)$ returns a value between 0, corresponding to a rotation of $\theta_i = 0$ degrees, and 1, corresponding to the maximum allowed rotation, which is set to 120 degrees. Abrupt changes in the direction of the movement are not only time consuming but also energy consuming. This is because UAV motors must apply enough force to counteract inertia and change direction. The worst-case scenario, with no restrictions, is a full 180-degree turn. The lower the result, the more efficient the waypoints are.

5) **Redundancy criterion:** $R(\theta_i)$ evaluates the trajectories generated by θ_i and returns how many cells of the grid decomposition of the area would be explored more than once. It is possible but not desirable for two different UAVs to visit the same location, losing information due to the opportunity cost. Again, the lower the result, the better the waypoints are.

D. AD HOC MONTE CARLO METHOD

This paper uses a Monte Carlo method to solve the minimisation problem. To avoid falling into local minima, the method works with the three best results of the objective function J, which are stored in J^*, a 3×1 vector. The combinations of angles that give these values are stored in θ^*, i.e., a $n_u \times 3$ matrix, being each column a vector $n_u \times 1$ with the angles θ_i of each UAV. These solutions must be at certain distances from each other, and these distances are stored in the 3×1 vector d_J. This distance criterion tries to avoid the local minima by forcing to search for solutions in other regions of the solution space of order $\mathbb{R}^{n_u}$. It is important to note that using more than the three best results to explore the entire solution space would be too time consuming.

The iterative process of finding the angles θ_i that yield the minimum value of J is shown in Fig. 7. The first step of the loop is to check the stop conditions. Since m is the cumulative number of solutions θ_i evaluated at any time, it cannot exceed the maximum number of evaluations, M. Similarly, t is the amount of time spent in the process and T is the maximum time allowed. Finally, c counts the iterations without significantly improving the objective function values, and C is the value that c cannot exceed. The percentage of objective function improvement that is considered significant is χ. If any of these conditions is not met, the loop ends and the solution is the first combinations of angles of the variable θ^*, i.e, $\theta^*(1)$.

If the loop continues, n solutions are going to be randomly generated and evaluated. The 3×1 vector R_J denotes the percentage of candidate solutions generated around each one of the three best solutions found so far, so multiplied by n gives the number of candidates around each solution, n_{θ_i}. Random angles generation has some limitations. Let the $n_u \times 1$ vector θ_0 be the current movement angle of each UAV, and the 3×1 vector θ_{lim} be the maximum allowed variation around each solution of θ^*. The random solution angles θ_{ci} must satisfy $\theta_{ci} \in [\theta^*(i) - \theta_{lim}(i), \theta^*(i) + \theta_{lim}(i)] \subseteq [\theta_0 - \Omega, \theta_0 + \Omega]$, where Ω is the maximum allowed angle variation over the movement angle of each UAV. In Fig. 7 only the generation of the angles of one UAV are shown for clarity.

Once the candidate solutions have been generated, they are evaluated in J. The new best solutions are chosen according to the distance criterion. In Fig. 7, around each one of the previous best solutions the circle bounded by the minimum distance at which the new best solutions must lie is plotted as Φ_i. In the example, the new minimum value of the objective function is obtained with θ_{c9}, which defines a new circle Φ_1. Although θ_{c12} gives the second minimum value of J, it cannot be selected because it is inside the circle Φ_1, so the angle θ_{c2} is chosen instead. Similarly, the previous best solution $\theta^*(1)$ is discarded in favour of θ_{c11}. If one of the best angles

$$
\begin{aligned}
\min_{\theta_i} J(\theta_i) &= \lambda_1 M_I(\theta_i) + \lambda_2 M_C(\theta_i) + \lambda_3 M_B(\theta_i) + \lambda_4 T(\theta_i) + \lambda_5 R(\theta_i) \\
\text{s.t.} \quad & 0 \le \theta_i \le \theta_{sup} \\
& x_{inf} \le x_i \le x_{sup} \\
& y_{inf} \le y_i \le y_{sup} \\
& x_{i+1} = x_i + v_i \cos\theta_i \\
& y_{i+1} = y_i + v_i \sin\theta_i, \\
& \forall i = 1, 2, \ldots, n_u
\end{aligned}
\tag{9}
$$

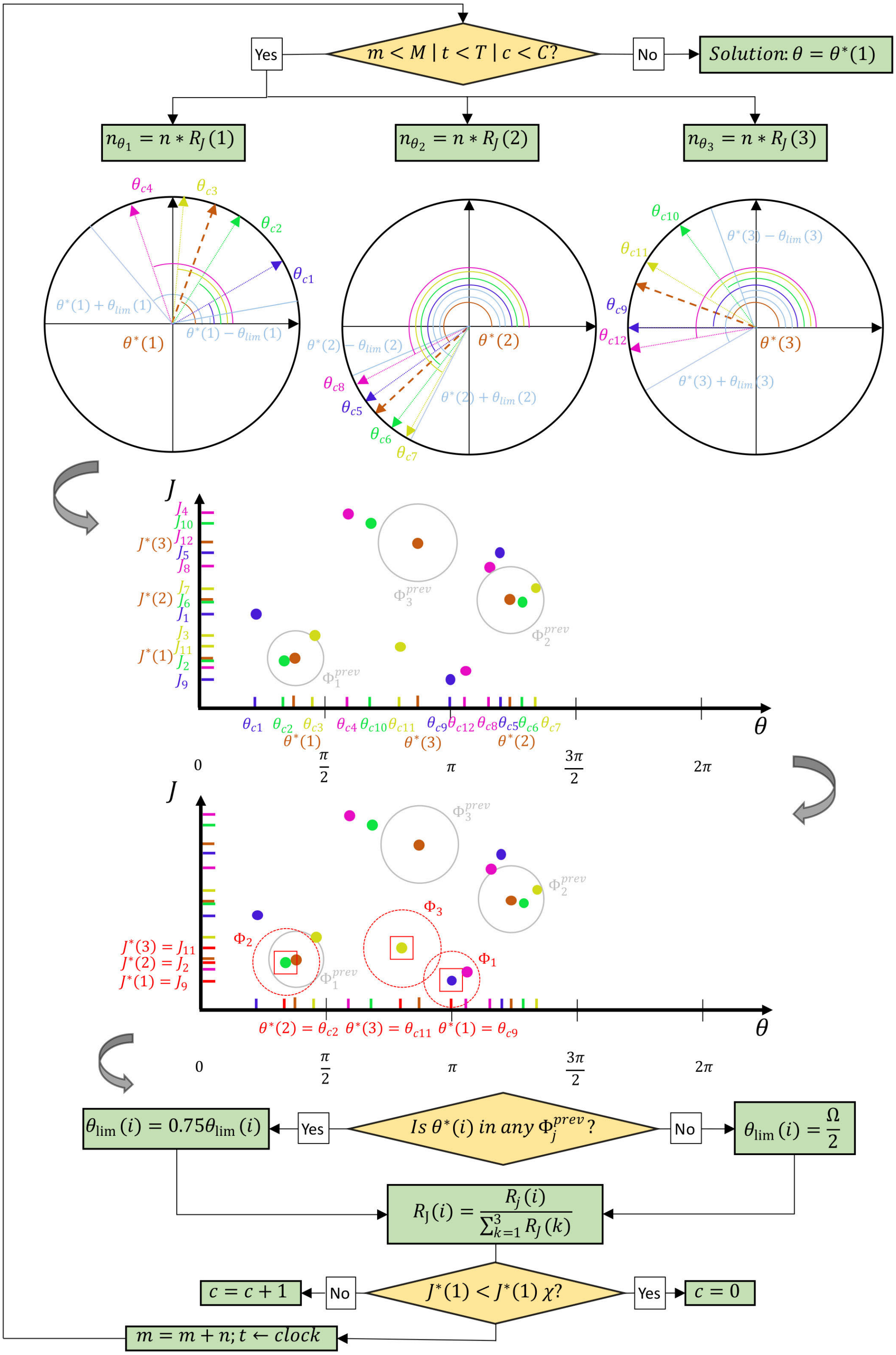
Yes
$m < M \mid t < T \mid c < C?$
No
$Solution: \theta = \theta^*(1)$
$n_{\theta_1} = n * R_J(1)$
$n_{\theta_2} = n * R_J(2)$
$n_{\theta_3} = n * R_J(3)$
θ_{c1} θ_{c2} θ_{c3} θ_{c4}
$\theta^*(1) + \theta_{lim}(1)$
$\theta^*(1) - \theta_{lim}(1)$
$\theta^*(1)$
$\theta^*(2) - \theta_{lim}(2)$
$\theta^*(2) + \theta_{lim}(2)$
$\theta^*(2)$
θ_{c5} θ_{c6} θ_{c7} θ_{c8}
θ_{c9} θ_{c10} θ_{c11} θ_{c12}
$\theta^*(3) - \theta_{lim}(3)$
$\theta^*(3) + \theta_{lim}(3)$
$\theta^*(3)$
J
J_4 J_{10} J_{12} J_5 J_8 J_7 J_6 J_1 J_3 J_{11} J_2 J_9
$J^*(3)$ $J^*(2)$ $J^*(1)$
Φ_3^{prev} Φ_2^{prev} Φ_1^{prev}
θ_{c1} θ_{c2} θ_{c3} θ_{c4} θ_{c10} θ_{c11} θ_{c9} θ_{c12} θ_{c8} θ_{c5} θ_{c6} θ_{c7}
$\theta^*(1)$ $\theta^*(3)$ $\theta^*(2)$
θ
0 $\frac{\pi}{2}$ π $\frac{3\pi}{2}$ 2π
J
Φ_3^{prev} Φ_2^{prev} Φ_1^{prev}
Φ_3 Φ_2 Φ_1
$J^*(3) = J_{11}$
$J^*(2) = J_2$
$J^*(1) = J_9$
$\theta^*(2) = \theta_{c2}$ $\theta^*(3) = \theta_{c11}$ $\theta^*(1) = \theta_{c9}$
θ
0 $\frac{\pi}{2}$ π $\frac{3\pi}{2}$ 2π
$\theta_{\lim}(i) = 0.75\theta_{\lim}(i)$
Yes
$Is\ \theta^*(i)\ in\ any\ \Phi_j^{prev}?$
No
$\theta_{\lim}(i) = \frac{\Omega}{2}$
$R_J(i) = \frac{R_J(i)}{\sum_{k=1}^{3} R_J(k)}$
$c = c + 1$
No
$J^*(1) < J^*(1)\,\chi?$
Yes
$c = 0$
$m = m + n; t \leftarrow clock$

FIGURE 7. Ad hoc Monte Carlo method representation.

$\theta^*(i)$ is inside a previous circle Φ_j, the maximum allowed variation θ_{lim} is decreased, otherwise it is increased to $\Omega/2$. The reason for this behaviour is that the previous circles are already explored and narrowing the limits gets a more precise search, whereas the new circles are unexplored and require a wider search angle.

Finally, the method updates the value of R_J, and the variables c, m and t that control the stop criteria, and repeats

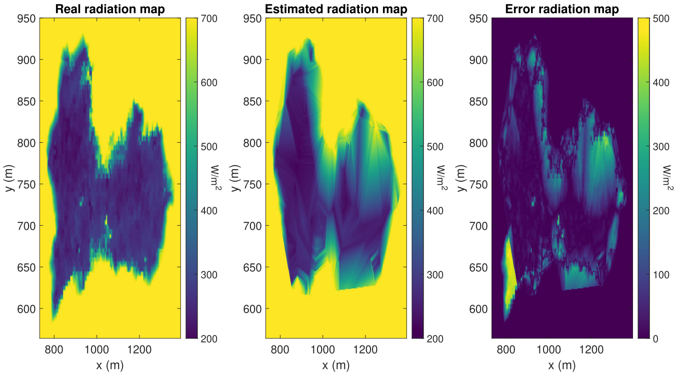

FIGURE 8. Estimated radiation map using the Delauney interpolation.

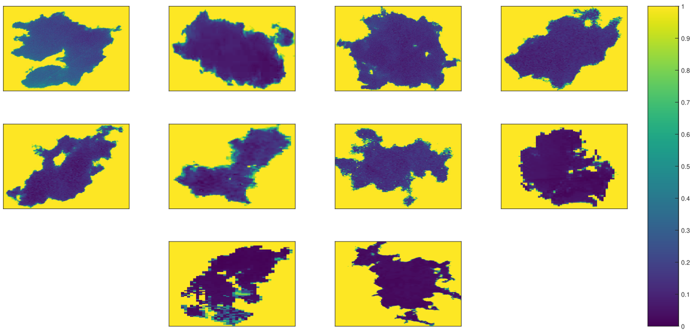

FIGURE 9. Possible cloud shapes.

TABLE 2. Parameters of the ad hoc Monte Carlo method.

Variable	n	M	T	C	χ	Ω	d_J
Value	30	900	0.9 s	5	0.5	120 degrees	$(1, 1.25, 1.5)^\intercal$

the process again. For the simulations of this paper, the values shown in Table 2 were used.

1) ESTIMATED RADIATION MAP

An estimated DNI map is produced from the RSS measurements. Delauney triangulation is used here to create a 2D linear interpolation and calculate the value of the unvisited cells in the map. This interpolation is well described in [27]. A result of this type of interpolation can be seen in Fig. 8, taken after the 3 UAVs have been describing the cloud shadow for almost 3 minutes. For a cloud of this size and using 3 UAVs a longer time is needed to obtain the final estimate, as it will be discussed later, but at this point the characteristic triangular shapes of the Delauney interpolation are noticeable.

IV. SIMULATION RESULTS

The proposed algorithm has been tested by simulations. Two hundred cases were randomly generated, each with the following properties:

- The ROI was a rectangular area measuring 1500 m by 1300 m. It was divided into a grid of 10 m by 10 m cells.
- The wind could blow in any direction. The wind speed was assumed to have a constant average value throughout the simulation, ranging from 1 m/s to 3 m/s.
- Clouds could have any of the 10 different shapes shown in Fig. 9. These shapes vary in their degree of similarity to an ellipse, concavity and number of holes. In each case, the clouds were randomly rotated between 0 degrees and 360 degrees, and also randomly scaled in length between 400 metres and 700 metres, relative to their longitudinal section. Finally, the clouds could be in any initial position as long as they crossed the ROI during their movement.
- The radiation value of a clear sky position was of 700 W/m^2. The threshold R_{cs} was set to 679 W/m^2 as the sensor error was assumed to be of 3%.
- Each one of the two hundred cases was tested three times, with 3, 5, and 7 UAVs, respectively. The constant average speed of the UAVs was assumed to be 8 m/s for horizontal movement and 2 m/s for vertical movement.

The global mean errors of the simulations are shown in Fig. 10. These errors are calculated using only the information in the shaded area, not the entire ROI. The time axis starts from the moment when the cloud was found. For example, using 3 UAVs, the global mean error dropped to about 110 W/m^2 200 seconds after the cloud was found, whereas the absolute mean error dropped to about 62 W/m^2 and 53 W/m^2 for the same period using 5 and 7 UAVs, respectively.

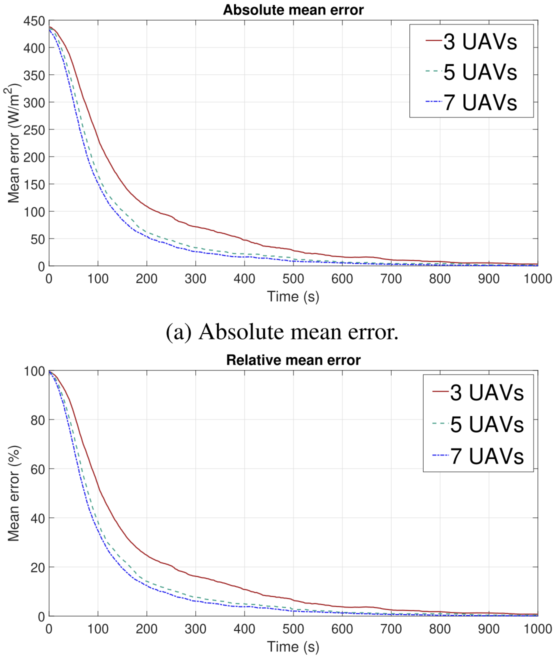

(a) Absolute mean error.

(b) Relative mean error.

FIGURE 10. Global mean errors of the simulated cases. Time axis refers to the time when the cloud was found.

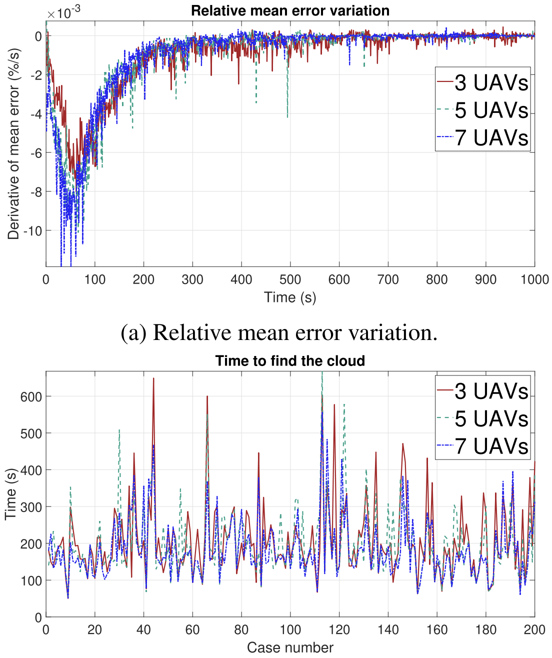

(a) Relative mean error variation.

(b) Time to find the cloud.

FIGURE 11. Comparison of variations in relative mean error and time taken to find the cloud in the simulated cases. Time axis refers to the time when the cloud was found.

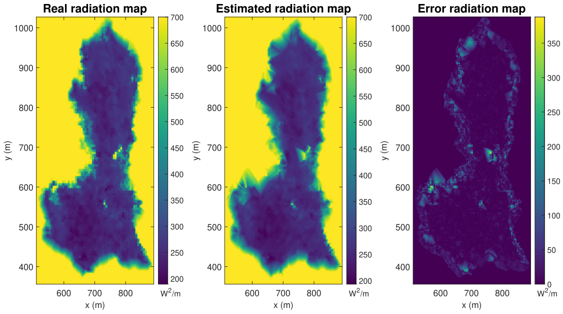

FIGURE 12. Final estimation of the cloud shadow. From left to right: real, estimated, and error radiation map.

It can be seen that there is a significant difference in the rate of error reduction between using 3 and 5 UAVs. However, there is not such a big difference between using 5 or 7 UAVs. Fig. 11a shows how the relative mean error decreases with different numbers of UAVs. After 100 or 200 seconds, the decrease ratio is very similar for the three cases, but before that the 3 UAVs team has a lower decrease ratio. For example, this difference results in a difference of almost 200 seconds for the 3 UAVs to reach errors below 50 W/m^2.

Fig. 11b shows the time to find the cloud using 3, 5, and 7 UAVs in each one of the simulated cases. The average times are 207 seconds, 196 seconds and 184 seconds respectively. Note that the team only knows the direction and speed of the cloud, with no indication of its position in the nearly 2 km^2 range, and that the horizontal speed of the UAVs only allows them to cover nearly 500 metres in one minute, explaining why the team typically takes 3 minutes to find the cloud.

The most problematic part of the shaded area for the algorithm are the boundaries. Due to the decomposition of the area, the boundary cells are more likely to have a higher error because they contain both clear and cloudy portions. As shown in Fig. 12, the errors in the boundaries can reach 100 W/m^2, whereas most of the region is below 20 W/m^2. Fig. 13 shows the mean error and the percentage of the area covered by the cloud shadow with an absolute error belonging to different error ranges. Fig. 13b is similar, but shows what percentage of the area is above or below the mean error. Both Fig. 13a and 13b refer to the case shown in Fig. 12. With 3 UAVs it takes 180 seconds to get most of the area under the mean error, but with 5 or 7 UAVs this time is halved. As can be seen, after 180 seconds, in the case of 5 or 7 UAVs, the mean error is around 50 W/m^2 or 40 W/m^2 respectively, but the 40% of the area has an error less than 10 W/m^2, and the 20% an error between 10 W/m^2 and 25 W/m^2.

A. COMPARISON WITH PREVIOUS ALGORITHM

We carried out another set of simulations to compare the results of the proposed algorithm with a previous method, specifically, with the algorithm explained in [28]. This algorithm assumes that the cloud has an elliptical shape and a blocking effect that behaves like a sigmoid function:

$$f(\delta) = \frac{1}{1 + e^{a_\sigma \delta + b_\sigma}} + c_\sigma, \tag{10}$$

where the parameters a_σ, b_σ, and c_σ specify the inflection point, slope, and the offset respectively, and δ is the normalised distance to the centre of the cloud.

First, we tested the proposed algorithm on a cloud that fulfilled the assumptions of the previous algorithm, i.e., with

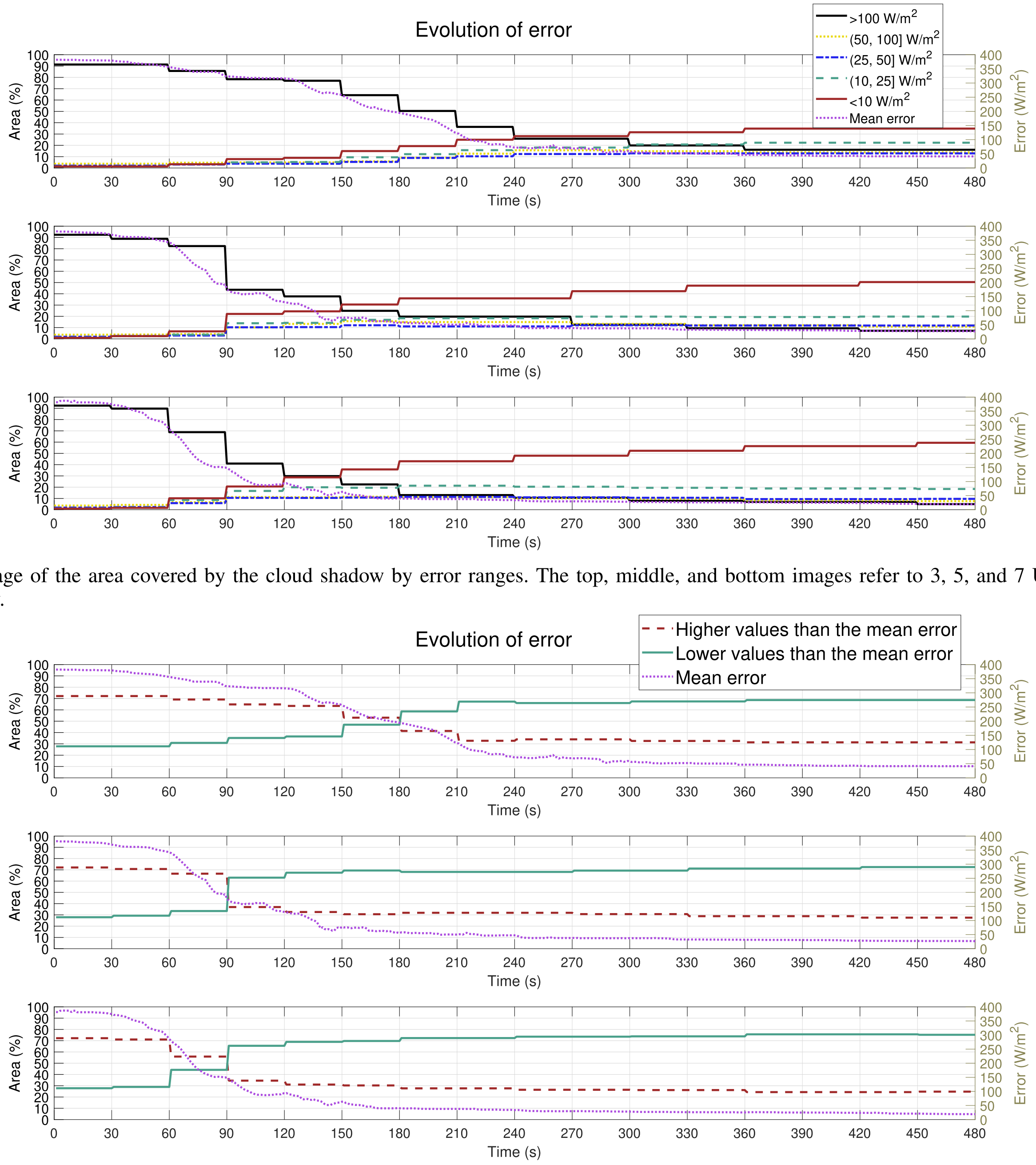

(a) Percentage of the area covered by the cloud shadow by error ranges. The top, middle, and bottom images refer to 3, 5, and 7 UAVs, respectively.

(b) Percentage of the area with higher or lower values than the mean error. The top, middle, and bottom images refer to 3, 5, and 7 UAVs, respectively.

FIGURE 13. **The time axis begins when the RSS finds the cloud shadow.**

an elliptical shape and the sigmoid function blocking effect behaviour. The cloud was the same one described in the above paper, with the following characteristics: 75 metres of semi-major axis, 40 metres of semi-minor axis, a rotation angle of 30 degrees, a speed of 1 metre per second and a movement direction $\overrightarrow{s} = (1, 0)$. We have also used the same number of UAVs for the test as in the previous work: 3, 6, and 12 UAVs teams.

The absolute mean errors obtained by both the previous and the proposed algorithms on this passing cloud can be seen in Fig. 14. Both algorithms converge in similar times, but the proposed algorithm achieves lower mean errors, around 10 W/m^2, whereas the previous one is around 40 W/m^2, so the new algorithm improves the previous one in a 75%. Fig. 15 depicts the estimated radiation map and its associated error map using the proposed algorithm.

Finally, we tested the same two hundred cases with the more realistic cloud shapes that we used to test the proposed algorithm with the previous algorithm. Fig. 16 shows the relative mean error with both algorithms. After 100 seconds,

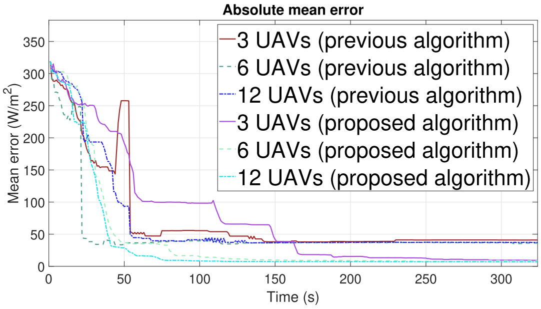

FIGURE 14. Absolute mean errors of the previous algorithm of the literature cloud case using this algorithm and the proposed algorithm.

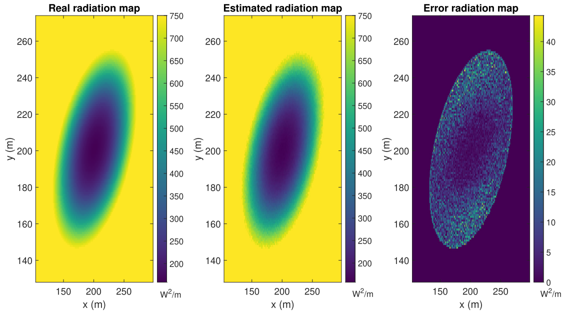

FIGURE 15. Estimation of the comparison cloud case blocking effect with the proposed algorithm. From left to right: real, estimated, and error radiation map.

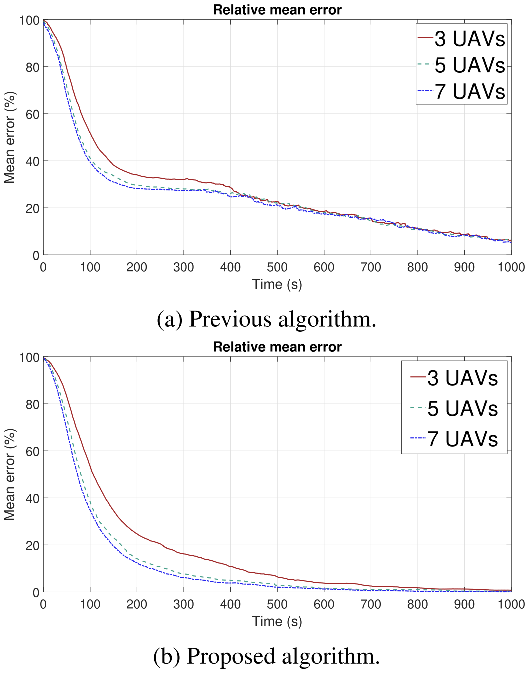

(a) Previous algorithm.

(b) Proposed algorithm.

FIGURE 16. Relative mean errors. Time axis refers to the time when the cloud was found.

both algorithms give similar results, but then the previous one decreases more slowly than the proposed one, taking more than 10 minutes to reach similar mean error values.

V. CONCLUSION

This paper presents an MPC-based algorithm for estimating the DNI of a region covered by a cloud shadow using an RSS, i.e. a group of UAVs equipped with light-weight and low power consumption sensors for DNI measurements. The algorithm manages the movement of the UAVs, generating waypoints for a time window by solving a minimisation problem, but only the first waypoints are used. The objective function includes several criteria such as the measurements taken and the efficiency in terms of energy consumption. A Monte Carlo method has been developed to solve the minimisation problem.

The proposed method has been tested with groups of 3, 5, and 7 UAVs and up to 10 different cloud shapes with random dimensions, orientation, and movement. All of them have provided a reliable description of the shadowed region, with the group of 3 UAVs being the slowest. With 7 UAVs, the algorithm gives a slightly better and faster description than with 5 UAVs. Despite the fact that the boundary of the shadowed region has an inherent error due to the grid decomposition of the area, the mean error drops below 50 W/m^2 after 5 minutes of description using 5 or 7 UAVs. Furthermore, the proposed algorithm has been shown to improve the results of a previous algorithm in terms of both efficiency and speed.

Future work involves addressing the current limitations of this proposal. Specifically, studying the proper tuning of the objective function weights under variable conditions, such as when the clouds move faster than 3 m/s or when their speed varies during detection. Another research direction to extend the capabilities of the current algorithm is to describe multiple clouds simultaneously and modify the problem formulation to address this scenario. In addition, it would be interesting to reduce the estimation time and to include in the formulation problem energy consumption models of the UAVs such as the one described in [29]. With this information, it would be possible to create energy-aware paths for the RSS and manage the fleet correctly, not sending the entire fleet into the field but only the minimum number of UAVs required. Finally, another line of research is to study the best control strategy of the parabolic trough plant with the spatial irradiance estimation given by this proposal.

REFERENCES

[1] T. S. Ledley, E. T. Sundquist, S. E. Schwartz, D. K. Hall, J. D. Fellows, and T. L. Killeen, "Climate change and greenhouse gases," *Eos, Trans. Amer. Geophys. Union*, vol. 80, no. 39, pp. 453–458, 1999.

[2] H. Chen, E. A. Tackie, I. Ahakwa, M. Musah, A. Salakpi, M. Alfred, and S. Atingabili, "Does energy consumption, economic growth, urbanization, and population growth influence carbon emissions in the BRICS? Evidence from panel models robust to cross-sectional dependence and slope heterogeneity," *Environ. Sci. Pollut. Res.*, vol. 29, no. 25, pp. 37598–37616, May 2022.

[3] A. Olabi and M. A. Abdelkareem, "Renewable energy and climate change," *Renew. Sustain. Energy Rev.*, vol. 158, Apr. 2022, Art. no. 112111.

[4] E. F. Camacho, A. J. Sánchez, and A. J. Gallego, *Solar Energy Systems: Progress and Future Directions* (Model Predictive Control of Large Scale Solar Trough Plants). Hauppauge, NY, USA: Nova Publishers, 2019, pp. 1–59.

[5] *A Policy Framework for Climate and Energy in the Period From 2020 up to 2030*, European Commission, Brussels, Belgium, 2014.

[6] E. Kabir, P. Kumar, S. Kumar, A. A. Adelodun, and K.-H. Kim, "Solar energy: Potential and future prospects," *Renew. Sustain. Energy Rev.*, vol. 82, pp. 894–900, Feb. 2018.

[7] F. Besharat, A. A. Dehghan, and A. R. Faghih, "Empirical models for estimating global solar radiation: A review and case study," *Renew. Sustain. Energy Rev.*, vol. 21, pp. 798–821, May 2013.

[8] I. Fountoulakis, P. Kosmopoulos, K. Papachristopoulou, I.-P. Raptis, R.-E. Mamouri, A. Nisantzi, A. Gkikas, J. Witthuhn, S. Bley, A. Moustaka, J. Buehl, P. Seifert, D. G. Hadjimitsis, C. Kontoes, and S. Kazadzis, "Effects of aerosols and clouds on the levels of surface solar radiation and solar energy in Cyprus," *Remote Sens.*, vol. 13, no. 12, p. 2319, Jun. 2021.

[9] G. A. Andrade, D. J. Pagano, J. D. Álvarez, and M. Berenguel, "A practical NMPC with robustness of stability applied to distributed solar power plants," *Sol. Energy*, vol. 92, pp. 106–122, Jun. 2013.

[10] A. J. Sánchez, A. J. Gallego, J. M. Escaño, and E. F. Camacho, "Temperature homogenization of a solar trough field for performance improvement," *Sol. Energy*, vol. 165, pp. 1–9, May 2018.

[11] *Ocontsolar Project Optimal Control of Thermal Solar Energy Systems*, European Commission, Brussels, Belgium, 2018.

[12] A. Sánchez-Amores, J. Martinez-Piazuelo, J. M. Maestre, C. Ocampo-Martinez, E. F. Camacho, and N. Quijano, "Coalitional model predictive control of parabolic-trough solar collector fields with population-dynamics assistance," *Appl. Energy*, vol. 334, Mar. 2023, Art. no. 120740.

[13] P. Kuhn, S. Wilbert, C. Prahl, D. Schüler, T. Haase, T. Hirsch, M. Wittmann, L. Ramirez, L. Zarzalejo, A. Meyer, L. Vuilleumier, P. Blanc, and R. Pitz-Paal, "Shadow camera system for the generation of solar irradiance maps," *Sol. Energy*, vol. 157, pp. 157–170, Nov. 2017.

[14] N. Minis, E. Rosenbluth, R. Hayut, and M. Am-Shallem, "Spatial DNI measurement for accurate solar flux control in megalim 121MWe solar receiver power plant," in *Proc. SOLARPACES Int. Conf. Concentrating Sol. Power Chem. Energy Syst.*, 2019, Art. no. 030037.

[15] F. Nex and F. Remondino, "UAV for 3D mapping applications: A review," *Appl. Geomatics*, vol. 6, no. 1, pp. 1–15, Mar. 2014.

[16] P. Radoglou-Grammatikis, P. Sarigiannidis, T. Lagkas, and I. Moscholios, "A compilation of UAV applications for precision agriculture," *Comput. Netw.*, vol. 172, May 2020, Art. no. 107148.

[17] K. Milidonis, A. Eliades, V. Grigoriev, and M. J. Blanco, "Unmanned aerial vehicles (UAVs) in the planning, operation and maintenance of concentrating solar thermal systems: A review," *Sol. Energy*, vol. 254, pp. 182–194, Apr. 2023.

[18] A. K. Gupta and P. J. Moss, *Guidelines for Design Low-Rise Buildings Subjected to Lateral Forces*. Boca Raton, FL, USA: CRC Press, 1993.

[19] M. S. Andreev, A. I. Chulichkov, A. P. Medvedev, and O. V. Postylyakov, "Estimation of cloud base height using ground-based stereo photography: Method and first results," *Proc. SPIE*, vol. 9242, pp. 335–341, Nov. 2014.

[20] OttHydroMet. (2023). *Lufft Ceilometer Series, Chm 15k and Chm 8k*. Accessed: Dec. 15, 2023. [Online]. Available: https://info.otthydromet.com/the_new_lufft_chm8k_ceilometer.html?utm_source=slider&utm_medium=microsite&utm_content&utm_campaign=2308_ott_c-met?_bk=ceilometer&_bm=p&_bt=657068446524&_bn=g&_bg=149421585075

[21] Solar MEMS Technologies. (2019). *Sun Sensor NANO-ISSX/c Technical Specifications*. Accessed: Aug. 18, 2020. [Online]. Available: http://www.solar-mems.com/smt_pdf/NANO_Technical_Specifications.pdf

[22] J. W. Spencer, "Fourier series representation of the position of the sun," *Search*, vol. 2, no. 5, p. 172, 1971.

[23] DJI Technology Inc. (2015). *Phantom 3 Pro User Manual*. Accessed: Jan. 18, 2021. [Online]. Available: https://dl.djicdn.com/downloads/phantom_3/en/Phantom_3_Professional_User_Manual__V1.6.pdf

[24] M. Larrañeta, A. Pérez-Gallego, M. A. Silva-Pérez, and I. Lillo-Bravo, "Cloudiness characterization in seville using ceilometer measurements," in *Proc. SOLARPACES Int. Conf. Concentrating Sol. Power Chem. Energy Syst.*, 2020, Art. no. 180003.

[25] G. Tselioudis, W. B. Rossow, and D. Rind, "Global patterns of cloud optical thickness variation with temperature," *J. Climate*, vol. 5, no. 12, pp. 1484–1495, Dec. 1992.

[26] J. M. Aguilar-Lopez, R. A. Garcia, and E. F. Camacho, "Shape detection algorithm applicable to solar estimation," *Revista Iberoamericana de Automática e Informática Ind.*, vol. 18, no. 3, pp. 277–287, 2021.

[27] I. Amidror, "Scattered data interpolation methods for electronic imaging systems: A survey," *J. Electron. Imag.*, vol. 11, no. 2, p. 157, Apr. 2002.

[28] J. M. Aguilar-López, R. A. García, A. J. Sánchez, A. J. Gallego, and E. F. Camacho, "Mobile sensor for clouds shadow detection and direct normal irradiance estimation," *Sol. Energy*, vol. 237, pp. 470–482, May 2022.

[29] J. M. Aguilar-López, R. A. García, C. Bordons, and E. F. Camacho, "Development of the energy consumption model of a quadrotor using voltage data from experimental flights," in *Proc. IEEE 17th Int. Conf. Control Autom. (ICCA)*, Jun. 2022, pp. 432–437.

JOSÉ M. AGUILAR-LÓPEZ was born in Osuna, Seville, Spain, in 1991. He is currently pursuing the Ph.D. degree in automation, robotics, and telematics with the Department of Systems and Automation Engineering, University of Seville. He is a Researcher for the ADG-ERC OCONTSOLAR Project. His research interests include UAVs, multi-agent system strategies and control, and solar DNI estimation.

RAMÓN A. GARCÍA was born in Seville, Spain, in 1985. He received the B.S. degree in industrial engineering with industrial automation specialization, the M.S. degree in automation, robotics, and telematics, and the Ph.D. degree in automatic control from the University of Seville, Spain, in 2011, 2013, and 2017, respectively. Since September 2018, he has been a Postdoctoral Researcher for the ERC Advanced Grant OCONTSOLAR with the University of Seville. His current research interests include set-membership algorithms, distributed estimation, control and multi-agent systems, and solar DNI estimation.

EDUARDO F. CAMACHO (Life Fellow, IEEE) received the Ph.D. degree in electrical engineering from the University of Seville. He is now an Emeritus Professor with the Department of System Engineering and Automatic Control, University of Seville. He has written the books: *Model Predictive Control in the Process Industry* (1995), *Advanced Control of Solar Plants* (1997), *Model Predictive Control* (Springer-Verlag, 1999 and 2004, second edition), *Control e Instrumentación de Procesos Químicos* (Ed. Síntesis), *Control of Dead-Time Processes* (2007), and *Control of Solar Energy Systems* (Springer-Verlag, 2012). He was appointed for four years as the Manager of the Advanced Production Technology Program of Spanish National Research and Development Program. He has acted as an evaluator of projects at national and European level. He was an Elected Member of the IEEE CSS Board of Governors, from 2008 to 2011. He was an IFAC Fellow, in 2009. He was recently awarded by European Research Council with an Advanced Grant. He has served on various technical committees of the International Federation of Automatic Control (IFAC). He chaired the IFAC Publication Committee, from 2002 to 2005, and the IFAC Policy Committee, from 2005 to 2011. He chaired the IEEE/CSS International Affairs Committee, from 2002 to 2005. He was the President of European Union Control Association, from 2005 to 2007. He was the Publication Chair of the IFAC World Congress b'02 and the General Chair of the joint 44 IEEE Control and Decision Conference (CDC) and European Control Conference (ECC), held in 2005, and the Co-General Chair of the joint 50 IEEE Control and Decision Conference (CDC) and European Control Conference (ECC), held in 2011. He has carried out review and editorial work for various conferences and technical journals. At present, he is one of the editors of *IFAC journal*, *Control Engineering Practice*, the Editor-at-Large of *European Journal of Control*, and a Subject Editor of *Optimal Control Applications and Methods*. He was one of the Spanish representatives of the Program Committee of the Growth Research Program and a National Expert of the Program Committee of the NMP Research Priority of European Union.